INTERNATIONAL JOURNAL FOR NUMERICAL METHODS IN FLUIDS, VOL. 14, 1391–1405 (1992)

IMPROVED ARTIFICIAL DISSIPATION SCHEMES FOR THE EULER EQUATIONS

M. P. THOMADAKIS AND S. TSANGARIS

Laboratory of Aerodynamics, National Technical University of Athens, PO Box 64070, 15710 Zografou, Athens, Greece

SUMMARY

The influence of artificial dissipation schemes on the accuracy and stability of the numerical solution of compressible flow is extensively examined. Using an implicit central difference factored scheme, an improved form of artificial dissipation is introduced which highly reduces the errors due to numerical viscosity. A function of the local Mach number is used to scale the amount of numerical damping added into the solution according to the character of the flow in several flow regimes. The resulting scheme is validated through several inviscid flow test cases.

KEY WORDS Artificial dissipation schemes Central difference schemes Compressible flow Euler equations

1. INTRODUCTION

The numerical solution of the equations that describe the motion of a compressible fluid has become commonplace in recent years. Time-marching numerical methods are usually implemented and many of them have been proven robust and accurate.

One of the most important properties that any method must possess is good damping behaviour, i.e. the ability to reduce the error towards zero as time increases to infinity while maintaining the accuracy of the solution within acceptable bounds. The damping behaviour of a scheme depends on the artificial dissipation, either inherent in the scheme, as in all classes of upwind schemes, or explicitly added, which is the case when central differencing is used.

Warming and Hyett[1] have introduced the 'modified equation approach' to examine the dissipative and dispersive properties of a numerical scheme. They suggest the transformation of the original differential equation by eliminating the time derivatives higher than first order, using any numerical scheme, to obtain the exact partial differential equation solved by the finite difference algorithm used. It is the right-hand-side terms of this modified equation that determine whether the numerical scheme is properly damping or not. They should contain even-order derivatives with the appropriate sign. Upwind schemes inherently provide this kind of terms, while central schemes do not and thus it is necessary to explicitly add them.

In this paper we shall consider only central differences. For that purpose we use one of the most popular implicit schemes of the last decade, which was introduced by Beam and Warming[2] and tested extensively in several kinds of flows.[3–5]

Any form of numerical damping is designed to accomplish two objectives. The first is to prevent the odd–even point decoupling due to phase errors from the solution and the second is to eliminate oscillations near the shock waves. The stronger the shock wave to be captured, the greater is the amount of dissipation needed to be added into the solution. Pulliam[6] and Jameson

0271–2091/92/121391–15$07.50

Received February 1991
Revised August 1992

et al.[7] used a blended non-linear form of second- and fourth-order artificial dissipation terms, while Swanson and Turkel[8] introduced some modifications to Jameson *et al.*'s model for better performance in multigrid calculations of flow problems around aerofoils.

Our previous experience[5,9] has shown that dissipation schemes can lead to false thick entropy layers near solid boundaries and stagnation points in inviscid flow and can cause instabilities in the solution of both viscous and inviscid flow problems. On the other hand, large amounts of artificial damping smear the shock waves, providing solutions of pour quality. Furthermore, the existing dissipation schemes are highly dependent on the computational grid used, being more dissipative on a highly stretched grid than on a smoother one. In the present study we introduce a procedure that improves the erroneous behaviour of numerical damping in a physical manner. The dominating role of the local Mach number is exploited and the result is an artificial dissipation scheme which provides only the necessary amount of dissipation, without destroying either the accuracy or the stability of the solution, and which seems to perform equally well on smooth as well as on highly skewed grids.

To isolate the role of artificial dissipation from the other characteristics of the numerical solution, we examine only inviscid flow cases in this work. This is done because the solution of the equations of an inviscid fluid provides accuracy criteria based on physical assumptions and excludes the influence of approximations such as the modelling of turbulence from the investigation. On the other hand, any conclusions concerning the stability and robustness of a numerical scheme derive from its performance in inviscid flow solution, where the absence of any physical dissipation clearly reveals its accuracy.

2. GOVERNING EQUATIONS AND NUMERICAL ALGORITHM

The equations used are the two-dimensional unsteady Euler equations, in conservative form, for a generalized curvilinear co-ordinate system. In their non-dimensional form they can be written as

$$\partial_t \mathbf{Q} + \partial_\xi \mathbf{F} + \partial_\eta \mathbf{G} = 0, \tag{1}$$

where

$$\mathbf{Q} = J^{-1}\begin{pmatrix} \rho \\ \rho u \\ \rho v \\ e \end{pmatrix}, \qquad \mathbf{F} = J^{-1}\begin{pmatrix} \rho U \\ \rho u U + \xi_x p \\ \rho v U + \xi_y p \\ (e+p)U - \xi_\tau p \end{pmatrix}, \qquad \mathbf{G} = J^{-1}\begin{pmatrix} \rho V \\ \rho u V + \eta_x p \\ \rho v V + \eta_y p \\ (e+p)V - \eta_\tau p \end{pmatrix}$$

are the vector of conservative variables and the convective fluxes respectively.

In the above expressions ξ and η are the curvilinear co-ordinates, which are related to the Cartesian co-ordinates x and y through the generalized co-ordinate transformation

$$\xi = \xi(x, y, \tau), \qquad \eta = \eta(x, y, \tau), \qquad t = \tau,$$

and $J = \xi_x \eta_y - \xi_y \eta_x$ is the Jacobian of the transformation. The Cartesian velocity components are denoted by u and v, ρ is the density and e is the specific total energy per unit volume. The pressure p and temperature T are given by the equations of state for a perfect gas. Finally, U and V are the contravariant velocities along the directions ξ and η respectively, given by

$$U = \xi_\tau + \xi_x u + \xi_y v, \qquad V = \eta_\tau + \eta_x u + \eta_y v.$$

The reference quantities are a reference velocity U_{ref}, a reference length L_{ref} and a reference density ρ_{ref} at some reference temperature T_{ref}. The reference value for time is then defined as

L_{ref}/U_{ref} and for the pressure and total energy as the product $\rho_{ref}U_{ref}^2$. The Mach number is defined as

$$M_\infty = \frac{U_{ref}}{\sqrt{(\gamma R T_{ref})}}.$$

The governing equations (1) are solved numerically following the method introduced by Beam and Warming.[2] We shall not go into details of the algorithm for reasons of brevity. We shall only outline the basic features of the scheme as it is implemented in the present study.

The generalized time differencing used is

$$\Delta \mathbf{Q}^n = \frac{\theta \Delta t}{1+\zeta}\frac{\partial}{\partial t}\Delta \mathbf{Q}^n + \frac{\Delta t}{1+\zeta}\frac{\partial}{\partial t}\mathbf{Q}^n + \frac{\zeta}{1+\zeta}\Delta \mathbf{Q}^{n-1} + O[(\theta - \tfrac{1}{2} - \zeta)\Delta t^2 + \Delta t^3]. \tag{2}$$

By simply varying the values of the coefficients θ and ζ in the above expression, a variety of temporal discretizations can be produced. For example, when $\theta = 1$ and $\zeta = 0{\cdot}5$ the three-point backward implicit scheme is obtained, when $\theta = 1$ and $\zeta = 0$ the Euler implicit scheme is derived and with $\theta = 0$ and $\zeta = 0$ the Euler explicit.

If equation (1) is solved for $\partial \mathbf{Q}/\partial t$ and the resulting expression is inserted in (2), if the flux vectors are linearized in the non-linear expression that occurs and if for the coupled system of equations the Approximate Factorization technique is used, then the following solution algorithm in delta formulation occurs:

$$\left(\mathbf{I} + \frac{\theta \Delta t}{1+\zeta}\mathbf{A}_\xi^n - \mathbf{D}_i^\xi\right)\Delta \mathbf{Q}^* = \mathrm{RHS} \tag{3a}$$

$$\left(\mathbf{I} + \frac{\theta \Delta t}{1+\zeta}\mathbf{B}_\eta^n - \mathbf{D}_i^\eta\right)\Delta \mathbf{Q}^n = \Delta \mathbf{Q}^*, \tag{3b}$$

$$\mathbf{Q}^{n+1} = \mathbf{Q}^n + \Delta \mathbf{Q}^n, \tag{3c}$$

with the right-hand side (RHS) of (3a) being given by

$$\mathrm{RHS} = \frac{\Delta t}{1+\zeta}(-\mathbf{F}_\xi^n - \mathbf{G}_\eta^n) + \frac{\zeta}{1+\zeta}\Delta \mathbf{Q}^{n-1} + \mathbf{D}_e + O[(\theta - \tfrac{1}{2} - \zeta)\Delta t^2 + \Delta t^3], \tag{3d}$$

where $\mathbf{I}$ denotes the identity matrix and $\mathbf{A}$ and $\mathbf{B}$ are the Jacobian matrices of $\mathbf{F}$ and $\mathbf{G}$ over $\mathbf{Q}$ respectively. Finally, $\mathbf{D}_i^\xi$ and $\mathbf{D}_i^\eta$ are the implicit damping operators in the directions ξ and η respectively, while $\mathbf{D}_e$ is the explicit dissipation term, which will be examined in detail in the following sections.

3. ARTIFICIAL DISSIPATION

Central differences are used for the discretization of the spatial derivative appearing in equations (3), so the explicit damping term $\mathbf{D}_e$ must be added to damp high-frequency oscillations. This term, as seen from equation (3d), modifies the equation that is actually solved. It must therefore be small in magnitude so that the overall second-order spatial accuracy is not destroyed. Furthermore, the implicit damping term $\mathbf{D}_i$ should be added in the implicit operators of equations (3) to extend the stability range of the solution and not to accelerate the convergence of the scheme.[10,11]

If the explicit damping term $\mathbf{D}_e$ consists only from fourth-order terms,[2,3] the scheme is proven unreliable for inviscid flow cases. The fourth-order terms fail to initialize the solution from free

stream values unless large values of the linear scaling coefficients are used, but even then spurious oscillations are present near the shock waves and the convergence rate decelerates by a factor of two or more.[11]

It is far more reliable to use the blended non-linear dissipation model that Jameson *et al.*[7] have introduced for a finite volume scheme and Pulliam[6] for a finite difference scheme:

$$\mathbf{D}_e = \nabla_\xi[\sigma^{(\xi)}_{i,j}(\varepsilon^{(\xi)(2)}_{i,j}\Delta_\xi J\mathbf{Q} - \varepsilon^{(\xi)(4)}_{i,j}\Delta_\xi\nabla_\xi\Delta_\xi J\mathbf{Q})] + \nabla_\eta[\sigma^{(\eta)}_{i,j}(\varepsilon^{(\eta)(2)}_{i,j}\Delta_\eta J\mathbf{Q} - \varepsilon^{(\eta)(4)}_{i,j}\Delta_\eta\nabla_\eta\Delta_\eta J\mathbf{Q})]. \quad (4)$$

In the above expression ∇_ξ, ∇_η and Δ_ξ, Δ_η are the backward and forward difference operators respectively, $\sigma^{(\xi)}$ and $\sigma^{(\eta)}$ are non-linear scaling coefficients intended to scale the whole dissipation terms by the local eigenvalues of the solution and $\varepsilon^{(2)}$ and $\varepsilon^{(4)}$ are coefficients used to switch from fourth- to second-order damping near the shock waves. The latter are given by the following expressions:

$$\varepsilon^{(\xi)(2)}_{i,j} = k_2\Delta t \max(\nu_{i+1,j}, \nu_{i,j}, \nu_{i-1,j}), \quad (5a)$$

$$\varepsilon^{(\eta)(2)}_{i,j} = k_2\Delta t \max(\nu_{i,j+1}, \nu_{i,j}, \nu_{i,j-1}), \quad (5b)$$

$$\varepsilon^{(\xi)(4)}_{i,j} = \max(0, k_4\Delta t - \varepsilon^{(\xi)(2)}_{i,j}). \quad (5c)$$

$$\varepsilon^{(\eta)(4)}_{i,j} = \max(0, k_4\Delta t - \varepsilon^{(\eta)(2)}_{i,j}), \quad (5d)$$

where k_2 and k_4 are constants and ν is a dissipation sensor. This sensor is defined as the gradient of a quantity directly related to the presence of a shock wave. As such, the normalized local second-order derivative of the pressure is used in present study:

$$\nu^{(\xi)}_{i,j} = \left|\frac{p_{i+1,j} - 2p_{i,j} + p_{i-1,j}}{p_{i+1,j} + 2p_{i,j} + p_{i-1,j}}\right|, \qquad \nu^{(\eta)}_{i,j} = \left|\frac{p_{i,j+1} - 2p_{i,j} + p_{i,j-1}}{p_{i,j+1} + 2p_{i,j} + p_{i,j-1}}\right|. \quad (6)$$

On the other hand, the usually implemented form of the scaling factors $\sigma^{(\xi)}$ and $\sigma^{(\eta)}$ is given by

$$\sigma^{(\xi)}_{i,j} = J^{-1}_{i,j}(\lambda^\xi_{i,j} + \lambda^\eta_{i,j}) + J^{-1}_{i+1,j}(\lambda^\xi_{i+1,j} + \lambda^\eta_{i+1,j}), \quad (7a)$$

$$\sigma^{(\eta)}_{i,j} = J^{-1}_{i,j}(\lambda^\xi_{i,j} + \lambda^\eta_{i,j}) + J^{-1}_{i,j+1}(\lambda^\xi_{i,j+1} + \lambda^\eta_{i,j+1}), \quad (7b)$$

where λ^ξ and λ^η are the largest eigenvalues of the Jacobian matrices **A** and **B** respectively:

$$\lambda^\xi_{i,j} = |U|_{i,j} + s\sqrt{(\xi_x^2 + \xi_y^2)}|_{i,j}, \qquad \lambda^\eta_{i,j} = |V|_{i,j} + s\sqrt{(\eta_x^2 + \eta_y^2)}|_{i,j}, \quad (8)$$

with s being the local speed of sound.

Careful observation of the above expressions leads to the following two important remarks.

The first is that the scaling factors of equations (7) give equal importance to both spatial directions, using the direct sum of both eigenvalues. This is equivalent to second-order upwind differencing, which switches to first-order near shock waves, and is effective on regular meshes with a cell aspect ratio close to unity. However, on fine grids with cell aspect ratios much greater than unity, adequate dissipation is added in one direction, while too much unnecessary damping is added in the other direction. This causes a loss of accuracy and may lead to false entropy layers in inviscid flow near solid boundaries. If the sum of eigenvalues is replaced by a directional scaling[8] of the form

$$\sigma^{(\xi)}_{i,j} = J^{-1}_{i,j}\lambda^\xi_{i,j} + J^{-1}_{i+1,j}\lambda^\xi_{i+1,j}, \qquad \sigma^{(\eta)}_{i,j} = J^{-1}_{i,j}\lambda^\eta_{i,j} + J^{-1}_{i,j+1}\lambda^\eta_{i,j+1}, \quad (9)$$

then instabilities may appear and oscillations near shock waves are excited.[11]

The second remark is that near shock waves the coefficient $\varepsilon^{(2)}$ takes rather large values owing to the large pressure gradients there, so that from equations (5c) and (5d) $\varepsilon^{(4)}$ drops to zero and hence only second-order dissipation is added. In smooth flow regions $\varepsilon^{(2)}$ should vanish and thus

only fourth-order dissipation should be added as background dissipation to prevent odd–even point decoupling. Unfortunately, the value of ν does not vanish away from shock waves, since the pressure gradient is non-trivial in other flow regions too, e.g. hear stagnation points and solid surfaces, especially when separation occurs in viscous flows. The same would happen if another quantity's derivative had been used, instead of pressure, for the definition of ν.[11]

The error due to highly skewed grids could be reduced by using a cell aspect ratio scaling of the whole dissipaton quantity $\mathbf{D}_e$,[12] but this would not prevent the erroneous behaviour of the dissipation scheme near stagnation points and within boundary layers.

As a physical and automated way to reduce the dissipation added in these flow regions, we propose the use of a Mach number function. The local Mach number is lower than the free stream Mach number in the stagnation region and higher upstream of a shock wave. It is also lower within low-speed regions, while it is of approximately the same size in regions of 'neutral' importance. We thus suggest that alternative expressions for both the scaling factor σ and the damping sensor ν should be used, multiplying them by an exponential function of the local Mach number.

In particular, equations (6) are modified into

$$\nu_{i,j}^{(\xi)}=\left(\frac{M_L}{M_\infty}\right)^a\left|\frac{p_{i+1,j}-2p_{i,j}+p_{i-1,j}}{p_{i+1,j}+2p_{i,j}+p_{i-1,j}}\right|, \qquad \nu_{i,j}^{(\eta)}=\left(\frac{M_L}{M_\infty}\right)^a\left|\frac{p_{i,j+1}-2p_{i,j}+p_{i,j-1}}{p_{i,j+1}+2p_{i,j}+p_{i,j-1}}\right|, \tag{10}$$

while equations (7) are modified into

$$\sigma_{i,j}^{(\xi)}=\left(\frac{M_L}{M_\infty}\right)^a\left[J_{i,j}^{-1}\left(1+\frac{\lambda^\eta}{\lambda^\xi}\right)_{i,j}^b\lambda_{i,j}^\xi+J_{i+1,j}^{-1}\left(1+\frac{\lambda^\eta}{\lambda^\xi}\right)_{i+1,j}^b\lambda_{i+1,j}^\xi\right], \tag{11a}$$

$$\sigma_{i,j}^{(\eta)}=\left(\frac{M_L}{M_\infty}\right)^a\left[J_{i,j}^{-1}\left(1+\frac{\lambda^\xi}{\lambda^\eta}\right)_{i,j}^b\lambda_{i,j}^\eta+J_{i,j+1}^{-1}\left(1+\frac{\lambda^\xi}{\lambda^\eta}\right)_{i,j+1}^b\lambda_{i,j+1}^\eta\right]. \tag{11b}$$

In the above equations M_L and M_∞ are the local and free-stream Mach numbers respectively, while a and b are user-specified constants. Note that either expressions (10) or expressions (11) are used, but not both simultaneously. The scaling with the Mach number has a dual effect. In inviscid flow the Mach number function reduces the amount of dissipation near the stagnation point while increasing the dissipation added near shock waves. In viscous flow an additional effect is that within a boundary layer, where the local Mach number is small, the numerical dissipation added is reduced, providing more accurate solutions.

It should also be noticed that the use of equations (10) is not expected to be equivalent to that of equations (11). The damping sensor ν is effective by intention near shock waves and by mistake near stagnation points and adverse pressure gradient regions. It is then expected to adjust the secon-order damping added and only thus increase the accuracy. On the other hand, the scaling factor σ acts over the whole damping term $\mathbf{D}_e$ and is expected to be more effective on accuracy. Furthermore, it contains a cell aspect ratio scaling of the eigenvalues,[8] which is important on skewed grids.

For the flow cases to be considered here, the constants that appear in the expressions above are held at the following constant values: $k_2=0{\cdot}25$, $k_4=0{\cdot}01$, $a=0, 1, 2$ and $b=0{\cdot}1$ (equations (10) and (11)).

Near computational boundaries the dissipation scheme should be modified so that the stability and accuracy are not disturbed. Since computations are performed on all internal grid points from $i=2$ to $i=i_{max}-1$ and from $j=2$ to $j=j_{max}-1$ and the second-order terms of equation (4) necessitate information from a three-point stencil, there is no difficulty in implementing the second-order terms to points near computational boundaries (i.e. $i=2$ or $i=i_{max}-1$). However,

when the fourth-order terms are considered, information is required at two neighbouring points on each side of the boundary grid point being considered. Therefore special treatment of these terms is needed for the first interior points. After an extensive examination of the various strategies that could be followed,[11] we have used second-order terms near the boundaries instead of fourth-order ones.

When the point $j=2$ is encoutnered, for example, we assume that

$$(JQ)_{i,j+1}-2(JQ)_{i,j}+(JQ)_{i,j-1}=\mathbf{0} \quad \text{at } j=2. \tag{12}$$

Then the expansion of equation (4) at $j=2$ is

$$\mathbf{D}^{\eta}_{i,2}=(\sigma_{i,3}+\sigma_{i,2})\{\varepsilon^{(\eta)(2)}_{i,2}[(JQ)_{i,3}-(JQ)_{i,2}]-\varepsilon^{(\eta)(4)}_{i,2}[(JQ)_{i,4}-3(JQ)_{i,3}+3(JQ)_{i,2}-(JQ)_{i,1}]\}$$
$$-(\sigma_{i,2}+\sigma_{i,1})\{\varepsilon^{(\eta)(2)}_{i,1}[(JQ)_{i,2}-(JQ)_{i,1}]-\varepsilon^{(\eta)(4)}_{i,1}[(JQ)_{i,3}-2(JQ)_{i,2}+(JQ)_{i,1}]\}. \tag{13}$$

The same treatment is followed at all computational boundaries. The terms multiplied by $\varepsilon^{(\eta)(4)}$ in equation (13) are second-order damping terms and provide almost the same high-frequency damping at boundaries as the interior fourth-order terms.[8, 11]

4. RESULTS AND DISCUSSION

4.1. Numerical implementation and boundary conditions

To validate the introduced form of artificial dissipation, three inviscid flow cases are considered.[13] In the present section only the most important findings of this investigation will be presented. For a more detailed discussion the reader is referred to Reference 11. These three inviscid cases are summarized in Table I.

The first-order Euler implicit scheme has been used ($\theta=1$ and $\zeta=0$ in equations (3)) for all computations. For the acceleration of the convergence a local time-stepping technique is employed. The local time step is given by

$$\Delta t=\frac{\Delta t_{\text{ref}}}{|U|+|V|+s\sqrt{(\xi_x^2+\xi_y^2+\eta_x^2+\eta_y^2)}}, \tag{14}$$

where Δt_{ref} is predefined.

The arbitrary curvilinear meshes used are generated by an elliptic solver developed by the authors following Sorenson.[14] Only C-type grids are considered, because in general the trailing edge point is a multivalued one and thus it should be treated as two distinct points, which is ensured by the use of C-type grids. The quality of the solution is then proved if the values of velocity at these two points differ in lifting cases while the static pressure values remain the same.

At the far-field boundary the local characteristic approach is used to define the Riemann invariants, either by extrapolation from the interior or by setting them equal to their free stream

Table I. Summary of test cases of present study on inviscid flow around NACA 0012, aerofoil[13]

No.	M_∞	α (deg)	Grid size	Wake points	Outer boundary distance (chords)
1	0·95	0	71×30	10	$-4\leqslant x\leqslant 5,\quad -5\leqslant y\leqslant 5$
	0·95	0	257×36	42	$-9\leqslant x\leqslant 10,\ -10\leqslant y\leqslant 10$
2	1·2	7	257×36	42	$-9\leqslant x\leqslant 10,\ -10\leqslant y\leqslant 10$
3	0·8	1·25	257×50	20	$-15\leqslant x\leqslant 15,\ -15\leqslant y\leqslant 15$

values according to the local subsonic or supersonic inflow or outflow. The same procedure is followed at the outflow boundary, but instead of the Riemann invariants the actual conservative variables are extrapolated or—when the flow is locally subsonic—the pressure is set equal to its free stream value. On the wake cut the conservative variables are obtained by averaging and for the fourth-order dissipation terms the same internal stencil is applied. Values from the other side of the wake cut are assigned to the necessary points from outside the domain.

On the aerofoil surface the normal momentum equation is used to define the pressure. The total enthalpy on the aerofoil is set equal to its free stream value. The tangential velocity is defined by extrapolation from the interor. We have examined several extrapolation strategies for the velocity.[11] The one found to introduce the minimum error in terms of total pressure loss is finally implemented in the present calculations. If the aerofoil is a ξ-line ($j=1$), V_t is the velocity tangential to the ξ-line at each point and V_n is the normal to this line velocity component, then

$$V_t = \mathbf{c} \cdot \frac{\mathbf{r}_\xi}{|\mathbf{r}_\xi|}, \qquad V_n = \mathbf{c} \cdot \frac{\nabla \eta}{|\nabla \eta|}, \tag{15}$$

where $\mathbf{c}=(u, v)^T$ is the velocity vector and $\mathbf{r}_\xi=(x_\xi, y_\xi)^T$ is the ξ-covariant base vector.

The tangential velocity on the solid surface is defined by projection of the tangential velocity component of the $j=2$ point, $\mathbf{V}_{t_2}$, on the direction tangent to the surface ($j=1$):

$$V_{t_1} = \mathbf{V}_{t_2} \cdot \frac{\mathbf{r}_{\xi_1}}{|\mathbf{r}_{\xi_1}|}. \tag{16}$$

For an impermeable stationary solid surface $V_{n_1}=0$ and thus the Cartesian velocity components are obtained by

$$u|_{j=1} = \frac{\eta_y V_{t_1}}{\sqrt{(\eta_x^2+\eta_y^2)}}, \qquad v|_{j=1} = -\frac{\eta_x V_{t_1}}{\sqrt{(\eta_x^2+\eta_y^2)}}. \tag{17}$$

For reasons of clarity in the subsequent discussion the following observations should be made. In all computations the form of the explicit damping was that of equation (4). When we refer to the use of equations (7) or (9), which are the forms of the scaling factor found in the literature, or (11), which is the form of σ introduced here, we imply that σ in equation (4) is defined by equations (7), (9) or (11) respectively. On the other hand, when we refer to the use of equations (10), we imply that ν of (10) is used to define the coefficients ε in equation (4).

4.2. Flow cases

The first case considered was the flow around the NACA 0012 aerofoil at $M_\infty=0{\cdot}95$ and $\alpha=0°$. For this non-lifting case on oblique shock wave appears on the trailing edge of the aerofoil and a second shock wave in the wake region. Two different grid sizes were used, a coarse 71×30 grid and a finer 257×36 grid (Figure 1). In terms of accuracy a comparison of the pressure coefficient, Mach number and total pressure loss on the aerofoil surface with those of Reference 13 is performed.

The total pressure loss on the aerofoil surface with the 71×30 grid is presented in Figure 2 for the three different scaling factors of equations (7), (9) and (11). The normal grid spacing on the aerofoil for this grid is 0·001 chords and the points are clustered towards the leading and trailing edges. The error in total pressure is far larger when equations (7) are used to define the scaling factor. It reduces significantly when the directional eigenvalues scaling of equations (9) is used, but oscillations are excited near the trailing edge. The error is significantly reduced, as are the oscillations near the shock, when the cell aspect ratio scaling of equations (11) with $a=0$ is used.

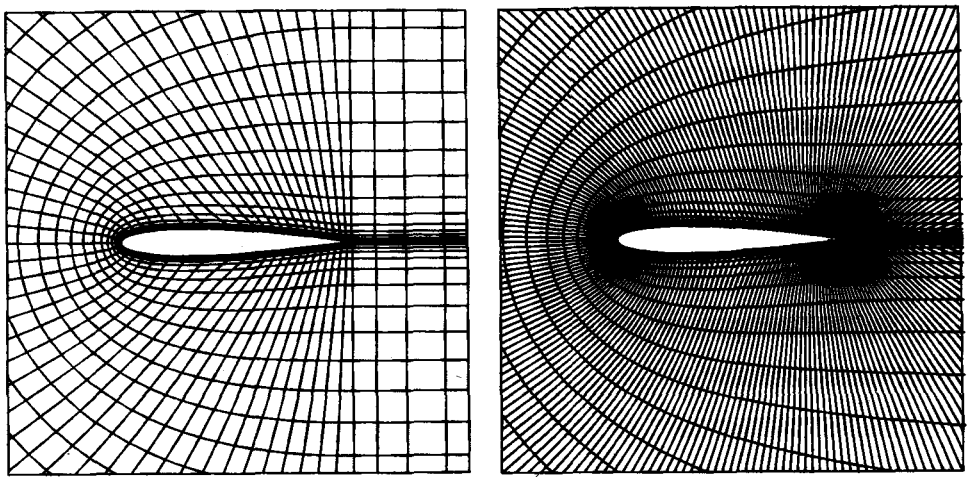

Figure 1. (a) Coarse (71 × 30) and (b) fine (257 × 36) C-type grids for inviscid flow. Enlargement near aerofoil

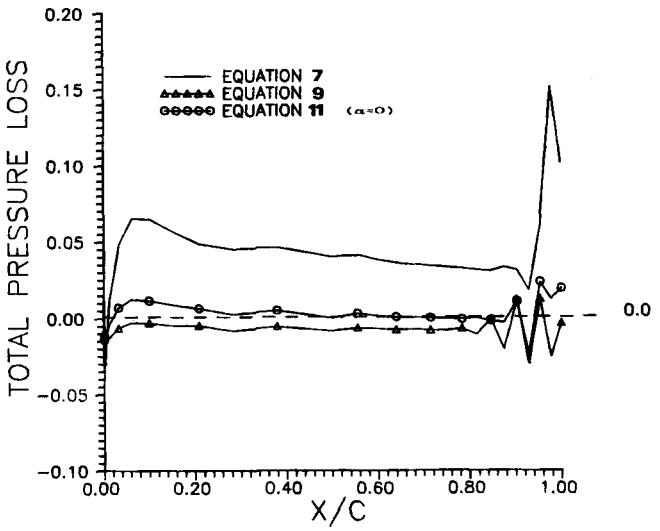

Figure 2. Total pressure loss on aerofoil surface for various damping scaling factors. $M_\infty = 0{\cdot}95$, $\alpha = 0°$, 71 × 30 grid

For the 257 × 36 grid the normal grid spacing is approximately 0·0005 chords and the points are also clustered towards the leading and trailing edges, thus leaving a rather sparse point distribution in the region $0.4 \leqslant x/c \leqslant 0{\cdot}6$. On this fine grid the relative performance of the introduced improvements of equations (10) and (11) is evaluated. As was previously mentioned, either equations (10) or (11) are used, but not both simultaneously. Their impact on the accuracy of the solution is clearly seen in Figure 3, where the total pressure loss on the aerofoil's surface is presented. It is obvious that a more accurate solution is obtained when scaling with the Mach number function is performed on the damping coefficient σ of equations (11) rather than on the

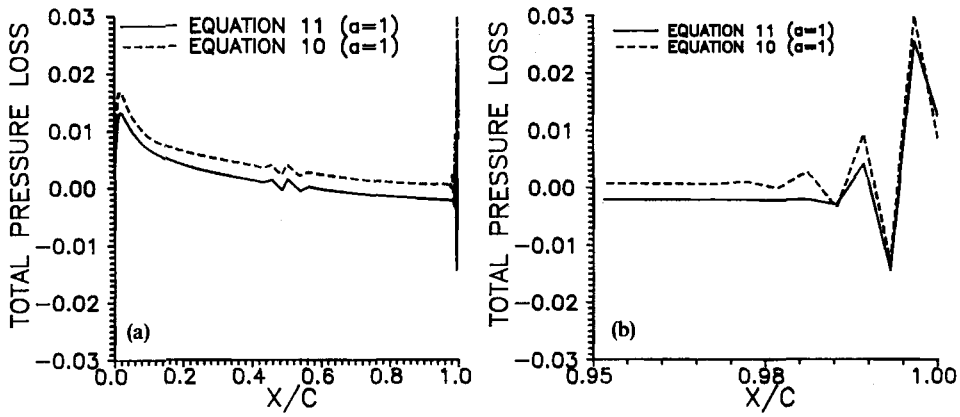

Figure 3. Comparison of influence that equations (10) and (11) have on accuracy: (a) surface distribution; (b) detail near trailing edge. $M_\infty = 0{\cdot}95$, $\alpha = 0°$, 257×36 grid

damping sensor ν of equations (10). Moreover, when the Mach number scaling is used in equations (11), oscillations near the trailing edge are less excited. We thus assume that using equations (11) is more effective than using equations (10).

In Figure 4 the influence of the exponent a on the accuracy is evaluated. For the same flow case, subsequent implementation of equations (11) is performed with different values of the exponent a. The minimum error is introduced when $a = 1$, except for the leading edge region, where using $a = 2$ is more accurate. The oscillations near the trailing edge shock wave are better damped when $a = 1$. This is due to the increased amount of dissipation added there because of the higher value of the Mach number function near the shock. As we shell see in the next case, the use of $a = 2$ is not reliable.

In Figure 5 the much higher accuracy that the introduced dissipation model provides over existing ones is clearly demonstrated. For the same fine grid the total pressure error that the damping coefficient of equations (7) causes is almost twice as large as the error which the new

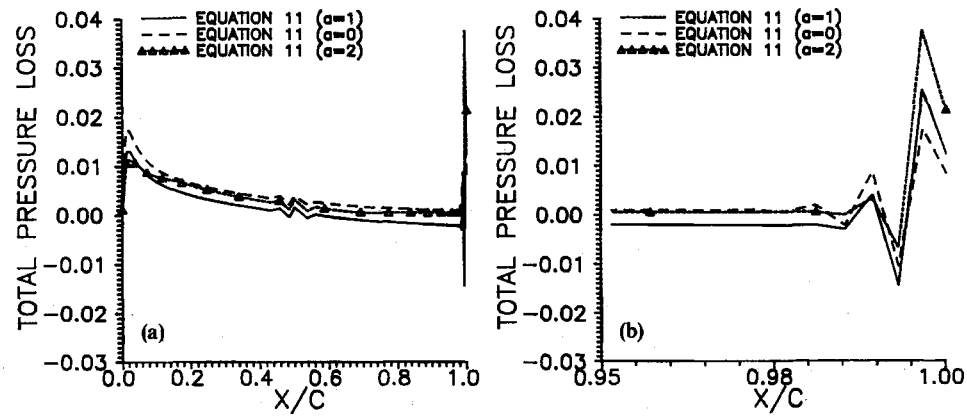

Figure 4. Effect on accuracy of exponent a: (a) surface distribution; (b) detail near trailing edge. $M_\infty = 0{\cdot}95$, $\alpha = 0°$, 257×36 grid

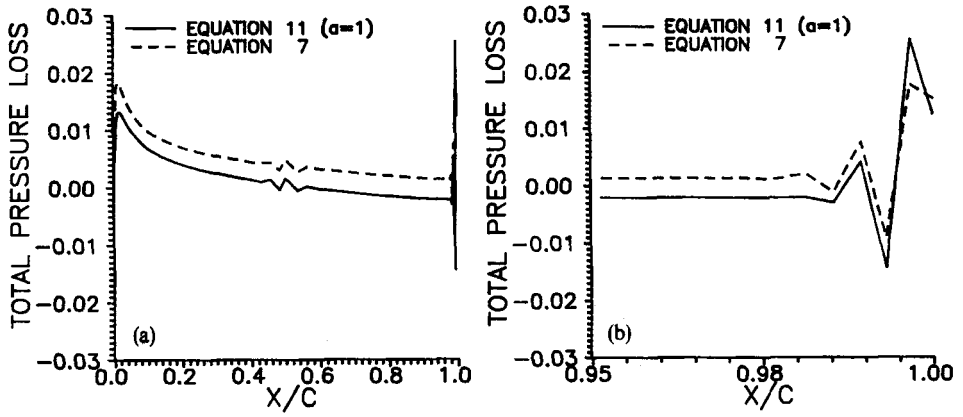

Figure 5. Total pressure loss on aerofoil surface for existing and improved damping scaling factors. $M_\infty = 0{\cdot}95$, $\alpha = 0°$, 257 × 36 grid

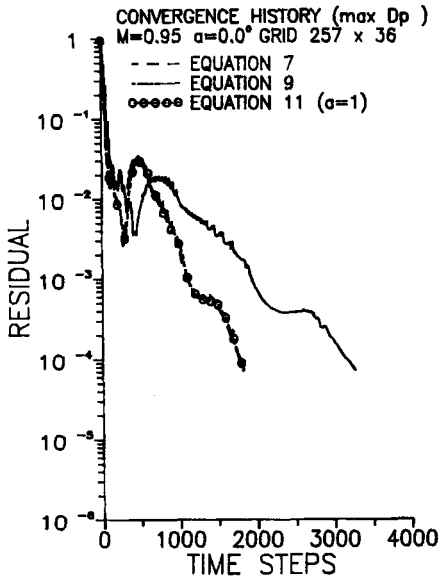

Figure 6. Convergence history on 257 × 36 grid for various damping scaling factors used. $M_\infty = 0{\cdot}95$, $\alpha = 0°$

scaling factor of equations (11) with $a = 1$ causes. A comparison with Figure 2 shows that the error which equations (7) introduce is much higher on coarse grids, while the error of equations (11) is almost the same on fine and coarse grids.

Although in most regions of the flow field reduced numerical viscosity is added with the new scheme, this does not affect the stability of the solution. This can be seen in Figure 6, where the convergence history of the present flow case is presented for the fine grid. As the convergence criterion the quantity $\max |\Delta\rho|^n$ is used. The implementation of either equations (7) or (11) with $a = 1$ has almost the same effect on convergence. In contrast, convergence is slower when equations (9) are used: a computer time increase of approximately 80% is observed. The

convergence rate when using $a=0$ or 2 in equations (11) is the same as when $a=1$ is used. This is not always ture, as will be shown in the following flow cases.

To conclude with the first flow case, the lines of constant Mach number in the flow field and the Mach number distribution on the aerofoil surface in comparison with the corresponding results of Reference 13 are presented in Figure 7. The iso-Mach lines were obtained using the improved dissipation of equations (11) with $a=1$. It must be noted here that the picture of the flow field does not vary from one dissipation scheme to another for this particular case.

For the second inviscid case considered, the free stream Mach number is 1·2 and the angle of attack is $\alpha=7°$. A detached bow shock appears before the leading edge and it would be interesting

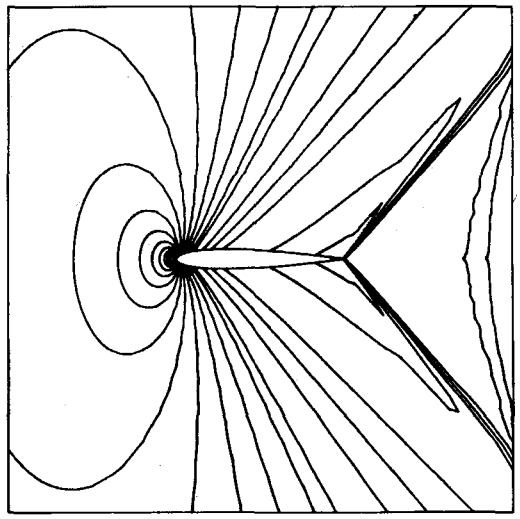

(a)

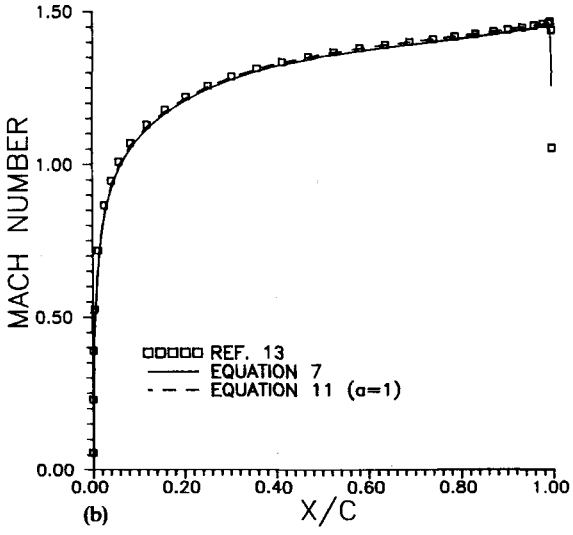

(b)

Figure 7. (a) Constant Mach number lines around NACA 0012 aerofoil ($\Delta M=0·05$). (b) Mach number distribution on aerofoil surface. $M_\infty=0·95$, $\alpha=0°$, 257×36 grid

to see the relative performance of the various manipulations of the dissipation there. It must be noted here that instabilities were observed when the scaling factor of equations (9) was used as well as when the new scaling of equations (11) with $a=2$ was used.

The most important finding in this particular case is that when the improved artificial dissipation scheme was used, the bow shock was captured more sharply. This can be seen in Figure 8, where the solutions obtained with the scaling of equations (7) (Figure 8(a)) and with the new scheme of equations (11) with $a=1$ (Figure 8(b)) are shown. This can also be verified from Figure 9(a), where the Mach number distribution on the upstream axis emanating from the leading edge to the inflow far-field boundary is shown. The use of equations (7) smears the bow shock over more grid points, while the shock is better captured with the scaling of equations (11) with $a=1$. The distribution of the Mach number on the aerofoil surface is shown in Figure 9(b). No appreciable differences between the solutions exist and the comparison with the solution of Reference 13 is very good. The differences that appear in the strength of the shock wave on the trailing edge in both the last two cases are due to the much denser grid of the best solution of Reference 13 (320 points on the aerofoil, against 173 of our solution). This comparison would be better if a denser grid was used in the present calculations or if the points were further clustered towards the trailing edge, but this would add nothing to the objective of this study and so was not performed.

Finally, the convergence history of this case is presented in Figure 10. This concerns only tose calculations which led to stable solution. It is obvious from this figure that the convergence rate for all the solutions is almost the same.

The last case that was tested was the flow at free stream Mach number 0·8 and incidence of 1·25°. The mesh used for this case consisted of 257×50 grid points and the outer boundary was located 15 chords away from the aerofoil. The normal grid spacing on the aerofoil surface was 0·00056 chords and the points on the surface were fairly equidistantly distributed. We are only going to present the Mach number and total pressure loss distributions on the aerofoil surface,

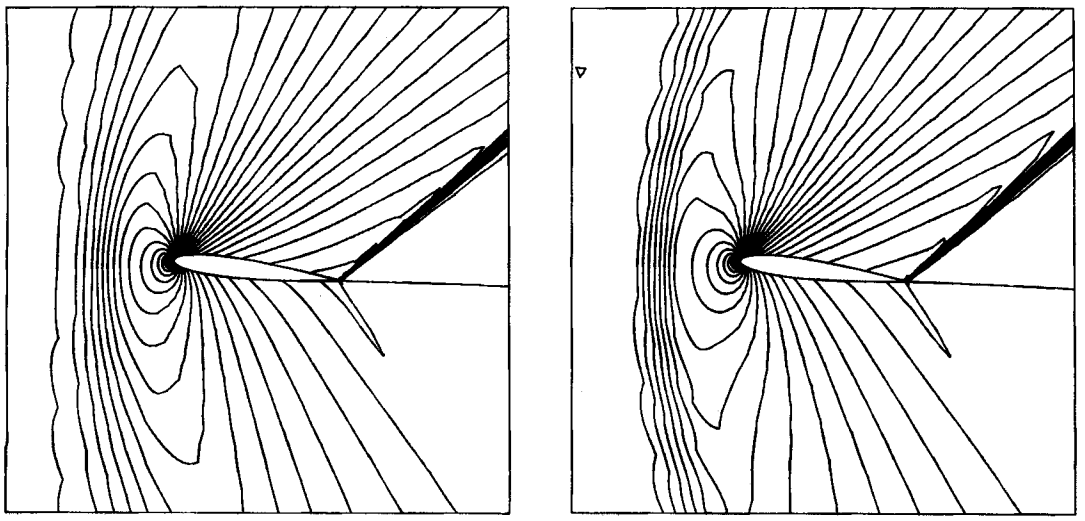

(a) (b)

Figure 8. Mach number contours around aerofoil for various scaling factors ($\Delta M=0{\cdot}05$). $M_\infty=1{\cdot}2$, $\alpha=7°$, 257×36 grid

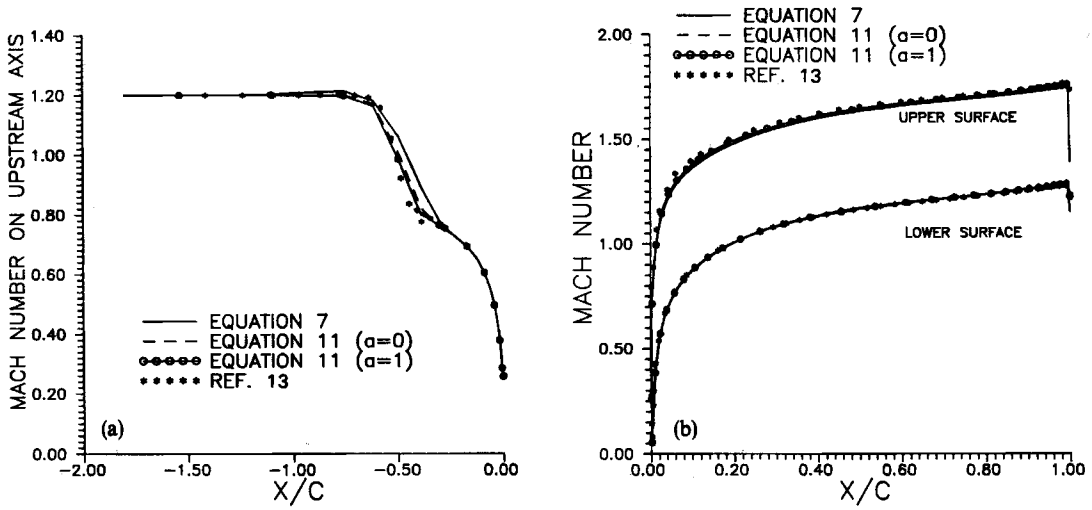

Figure 9. Mach number distribution on (a) upstream axis and (b) aerofoil surface for various dissipation forms. $M_\infty = 1{\cdot}2$, $\alpha = 7°$

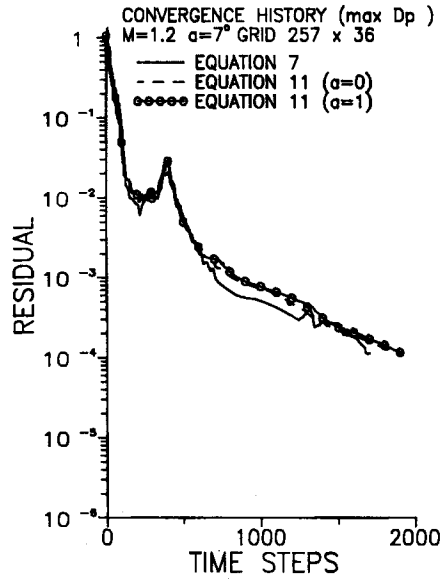

Figure 10. Convergence history on 257 × 36 grid for various damping scaling factors used. $M_\infty = 1{\cdot}2$, $\alpha = 7°$, 257 × 36 grid

and these only for the scaling of equations (7) and (11). Figure 11 shows the former distributions while Figure 12 presents the latter for $a = 1$. A simple comparison of the two figures shows clearly that the introduced dissipation scheme provides sharper shock waves on both the upper and lower surfaces of the aerofoil. At the same time the error on the total pressure is *five times* smaller when the improved scheme is used. It must be noted that when we set $a = 2$ in equations (11), instabilities were also observed. This proves that the standard value of a should be $a = 1$ for robust

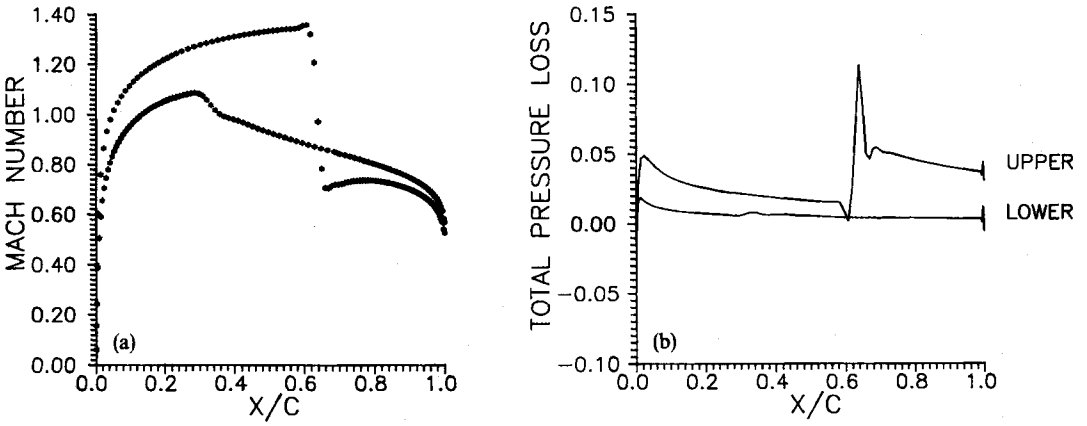

Figure 11. (a) Mach number and (b) total pressure loss distributions on aerofoil surface for scaling factor of equations (7). $M_\infty = 0{\cdot}8$, $\alpha = 1{\cdot}25°$, 257×50 grid

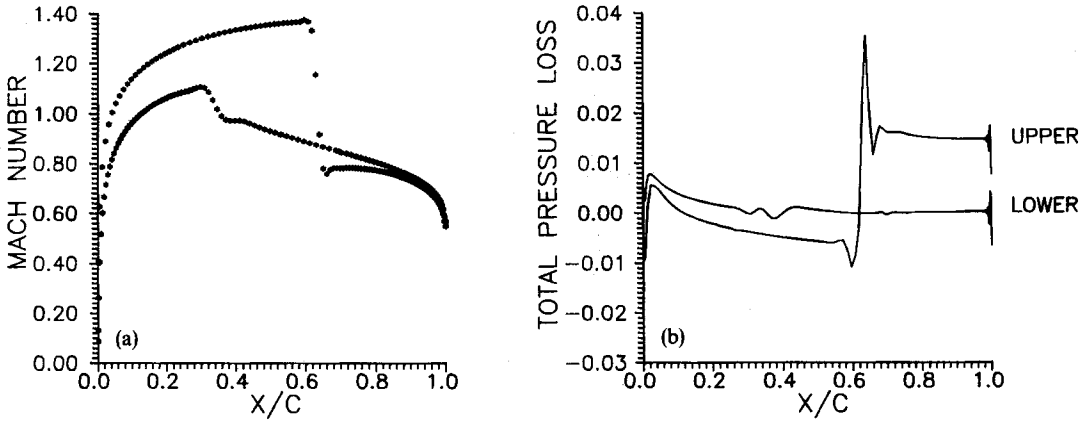

Figure 12. (a) Mach number and (b) total pressure loss distributions on aerofoil surface for scaling factor of equations (11) with $a = 1$, $M_\infty - 0{\cdot}8$, $\alpha = 1{\cdot}25°$

performance of the new dissipation scheme. We assume that the instabilities observed when $a = 2$ are due to the very small amount of dissipation that is added, which turns the solution unstable. The solution converged for all other values of a as well as for all the other dissipation scaling factors.

5. CONCLUSIONS

An improved artificial dissipation scheme is introduced in the present study and its enhanced properties are validated through numerical experiments for inviscid flows around aerofoils. The main advantages that the use of the new form of artificial dissipation offers can be summarized as follows.

1. The amount of numerical viscosity used by the driving scheme is automatically scaled by a local Mach number function.

2. The accuracy of the solution is improved near solid surfaces and stagnation points. For a given grid the error can be reduced by as much as five times compared to the error that existing dissipation schemes cause.
3. The shock waves are captured within less grid points and the oscillations near them are greatly reduced.
4. The error in the solution is equally small on coarse and fine grids, while for existing schemes the error is much greater on coarse grids and can be reduced only by grid refinement.
5. The amount of dissipaton added into the solution is correctly scaled for every cell aspect ratio. It is efficient on both smooth and highly skewed grids.

The promising performance of the improved scheme in inviscid flow calculations is expected to be of great importance of viscous calculations also. Its accurate performance on skewed grids as well as in regions of low speed would be very useful for the accurate numerical resolution of boundary layers and separation regions.

REFERENCES

1. R. F. Warming and B. J. Hyett, 'The modified equation approach to the stability and accuracy analysis of finite-difference methods', *J. Comput. Phys.*, **14**, 159–179 (1974).
2. R. M. Beam and R. F. Warming, 'An implicit factored scheme for the compressible Navier–Stokes equations', *AIAA J.*, **16**, 393–402 (1978).
3. J. L. Steger, 'Implicit finite difference simulation of flow about arbitrary two dimensional geometries', *AIAA J.*, **16**, 679–685 (1978).
4. T. H. Pulliam and J. L. Steger, 'Implicit finite difference simulation of three dimensional compressible flow', *AIAA J.*, **16**, 159–167 (1980).
5. M. P. Thomadakis and S. Tsangaris, 'Full Navier–Stokes solutions on personal computers', *Proc. 3rd Int. Congr. of Fluid Mechanics, Vol. 2*, Cairo, 1990, pp. 501–516.
6. T. H. Pulliam, 'Artificial dissipation models for the Euler equations' *AIAA J.*, **24**, 1931–1940 (1986).
7. A. Jameson, W. Schmidt and E. Turkel, 'Numerical solutions of the Euler equations by finite volume methods using Runge–Kutta time-stepping schemes', *AIAA Paper 81-1259*, 1981.
8. R. C. Swanson and E. Turkel, 'Artificial dissipation and central difference schemes for the Euler and Navier–Stokes equations', *AIAA Paper 87-1107-CP*, 1987.
9. M. P. Thomadakis and S. Tsangaris, 'Viscous flow around an airfoil including wall effects', *ZAMM*, **71**, T450–T452 (1991).
10. T. H. Pulliam, Efficient solution methods for the Navier–Stokes equations', *VKI Lecture Series*, 1986.
11. M. P. Thomadakis and S. Tsangaris, 'The impact of artificial dissipation models on the numerical simulation of compressible flows', *NTUA Report*, January 1991.
12. L. Martinelli, 'Calculation of viscous flows with multigrid methods', *Ph.d. Dissertation*, Princeton University, 1987.
13. 'Test cases for inviscid flow field methods', *AGARD-AR-211*, 1985.
14. R. L. Sorenson, 'A computer program to generate two dimensional grids about airfoils and other shapes by the use of Poisson's equation', *NASA TM-81198*, 1981.